ADVANCED FUNCTIONAL MATERIALS
www.afm-journal.de

# Protophilic $TiO_x/Ti_3C_2T_z$ Nanosheets for Hyper-Efficient Closed-Loop Pd Recycling

*Youngkyun Jung, Shi-Hyun Seok, Minki Jun, Kyung-Seok Lee, Yun Lee, Seungchul Kim, Keunsu Choi,* Jin Young Kim,* and Jae-Woo Choi**

**Sustainable recovery and upcycling/recycling of palladium (Pd) remain critical challenges for industrial competitiveness and environmental protection. However, conventional adsorbents struggle to provide efficient solutions due to their limited performance across diverse pH conditions. Herein, protophilic is presented $TiO_x/Ti_3C_2T_z$ nanosheets (NSs) engineered by incorporating unsaturated titanium oxide ($TiO_x$) nanoclusters, which revolutionize Pd recovery through a unique adsorption–redox mechanism. The $TiO_x/Ti_3C_2T_z$ NSs exhibit a high maximum Pd(II) adsorption capacity of 1983.3 mg $g^{-1}$ and achieve ≈100% recovery efficiency even at ultra-trace concentrations of 100 µg $L^{-1}$. Their exceptional protophilicity and strong reducing capability ensure selective Pd(II) reduction to Pd(0) over a wide pH range, followed by fusion-induced precipitation into large particles that are easily separable by filtration. The NSs retain over 98.7% of their performance after a regeneration cycle, confirming excellent structural stability and reusability. Notably, Pd-loaded NSs function as efficient electrocatalysts for hydrogen evolution, achieving a low overpotential of 39 mV at −10 mA $cm^{-2}$ and a mass activity of 0.19 A $mg^{-1}$, comparable to commercial Pd/C catalysts. This breakthrough establishes a new paradigm for sustainable precious metal recovery, strengthening global resource security and advancing the circular economy.**

## 1. Introduction

Palladium (Pd) plays a vital role in modern technology and the chemical industry owing to its exceptional catalytic properties. It is extensively used in cross-coupling reactions such as Sonogashira, Suzuki, Negishi, Heck, Buchwald–Hartwig, and Stille reactions.[1–3] Moreover, the remarkable chemical stability and high catalytic activity of Pd make it a promising catalyst for electrocatalytic processes, including the hydrogen evolution reaction (HER), formic acid oxidation, and ethanol oxidation.[4,5] However, the high cost of Pd significantly limits its widespread application in sustainable industrial processes.[6,7] In addition to its economic value, Pd has also emerged as an environmental concern due to its toxicity and potential for bioaccumulation in ecosystems and human tissues.[8] The finite nature of Pd reserves poses significant challenges, including high energy demands and environmental degradation.

Y. Jung, K.-S. Lee, Y. Lee, J.-W. Choi
Center for Water Cycle Research
Korea Institute of Science and Technology (KIST)
Seoul 02792, Republic of Korea
E-mail: plead36@kist.re.kr

S.-H. Seok, M. Jun, J. Y. Kim
Center for Hydrogen and Fuel Cells
Korea Institute of Science and Technology (KIST)
Seoul 02792, Republic of Korea
E-mail: jinykim@kist.re.kr

K.-S. Lee, Y. Lee
Department of Chemical and Biological Engineering
Korea University
Seoul 02841, Republic of Korea

S. Kim
Computational Science Research Center
Korea Institute of Science and Technology (KIST)
Seoul 02792, Republic of Korea

K. Choi
Department of Physics
Ulsan National Institute of Science and Technology (UNIST)
Ulsan 44919, Republic of Korea
E-mail: ubercgs@unist.ac.kr

K. Choi
Quantum Intelligence Corporation
Seoul 07326, Republic of Korea

J. Y. Kim, J.-W. Choi
Division of Energy & Environment Technology
KIST School
Korea National University of Science and Technology (UST)
Seoul 02792, Republic of Korea

The ORCID identification number(s) for the author(s) of this article can be found under https://doi.org/10.1002/adfm.202511809



**DOI: 10.1002/adfm.202511809**

Natural ores contain extremely low concentrations of Pd (≈10 g per ton).[9] With an annual global production of ≈215 tons,[10] traditional extraction processes are highly carbon-intensive, releasing ≈3.88 tons of $CO_2$ per kg of Pd produced.[11,12] Furthermore, the uneven global distribution of Pd resources exacerbates the supply–demand imbalance.[13] Consequently, recovering Pd from secondary sources has become an essential strategy for sustainable recycling and catalytic upcycling.

Among hydrometallurgical methods such as adsorption,[14] membrane filtration,[15] photocatalysis,[16] and electrochemical treatment,[17] adsorption-based Pd recovery is preferred owing to its safety, simplicity, and high efficiency at low Pd concentrations.[18] For sustainable, closed-loop Pd recycling, adsorbents must selectively recover Pd from complex matrices containing suspended solids and co-existing ions. Furthermore, the ability to reduce Pd(II) ions to Pd nanoparticles (NPs) on the adsorbent surface is critical for enhancing adsorption capacity, facilitating catalytic upcycling, and minimizing Pd usage. The reusability of the adsorbent further enhances its economic and environmental viability, allowing high-purity Pd to be recovered over multiple cycles.

Pd adsorbents incorporating nitrogen, oxygen, and/or sulfur functionalities—such as transition metal carbides and nitrides (MXenes),[19] polymers,[20] silica-based materials,[21] covalent organic framework,[22] and metal–organic frameworks[23]—have been extensively studied. Under acidic conditions (pH < 2), like a leachate of spent Pd catalysts, most materials selectively adsorb Pd(II) ions through electrostatic interactions.[24,25] However, at slightly higher pH levels (pH > 2), deprotonation of surface groups reduces their adsorption efficiency in industrial wastewater environments.[26]

To improve the adsorption selectivity for Pd(II) ions, which primarily exist as $PdCl_4^{2-}$ complexes under mildly acidic conditions,[27] positively charged adsorbent surfaces—achieved via protonation—are commonly employed. Controlling crystallinity and size of $TiO_2$ can increase protophilicity by promoting the formation of unsaturated oxygen atoms. However, their weak binding force of these oxygen sites for $PdCl_4^{2-}$, along with the requirement for sub-nanometer structural control, limits their practical applicability and raises concerns regarding secondary pollution and resource loss. As an alternative, 2D MXenes allow for the controlled generation of unsaturated oxygen atoms via HF etching, thereby enhancing Pd(II) adsorption affinity across a wide pH range. Among various MXene families, $Ti_3C_2T_x$ is the most widely studied due to its well-established synthesis protocols, high surface functionality density, and superior oxidation resistance. Compared to $Mo_2TiC_2T_x$ or $Nb_2CT_x$, which have shown limited Pd loading capacity (e.g., 4.27 at.% for Pd@$Mo_2TiC_2T_x$), $Ti_3C_2T_x$ offers denser –O and –OH terminations that enhance $PdCl_4^{2-}$ adsorption and reduction. Owing to their strong reduction capacity and large surface area,[28,29] we hypothesize that fine-tuning the oxygen coordination environment in MXenes enables efficient extraction of high-purity Pd from complex mixtures. Furthermore, the in-situ formation of Pd NP-decorated MXene composites significantly enhances their adsorption capacity and selectivity. Meanwhile, MXenes have garnered significant attention as catalyst supports due to their intrinsic properties, including high (electro)chemical stability.[30–32] When MXene and metal particles form a heterostructure, the strong interaction between the functional groups and vacancies on the surface of MXene and the metal particles induces catalytic activity modulation and increased stability.[30,33,34] Therefore, the prepared MXene decorated with HER-active Pd NP has sufficient potential to exhibit superior electrocatalytic activity and stability without an additional synthetic process.

In this study, we propose an MXene nanosheet (NS) utilizing unsaturated titanium dioxide ($TiO_x$) nanocluster-anchored $Ti_3C_2T_z$ ($TiO_x/Ti_3C_2T_z$). The material exhibits exceptional adsorption–reduction capabilities for $PdCl_4^{2-}$ across a broad pH range, demonstrating highly selective, rapid, and energy-efficient Pd recovery. The strong reducing ability of the NSs facilitates the spontaneous reduction of Pd(II) to Pd(0) NPs, followed by intermolecular fusion that generates large precipitates readily separable from the solution. Unsaturated oxygen atoms introduce a substantial positive surface potential, further improving Pd adsorption efficiency and promoting fusion-induced precipitation. Additionally, Pd-adsorbed NSs (Pd/NSs) can be directly utilized as electrocatalysts for HER in hydrogen purification and storage or regenerated for repeated use in Pd recovery.

## 2. Results and Discussion

### 2.1. Physicochemical Properties

Harsh HF conditions were required to exfoliate $Ti_3C_2T_z$ layers (**Figure 1a**) from $Ti_3AlC_2$ powders. However, these acidic conditions degraded the electronic properties of the resulting material by generating unsaturated (Figure 1b) or saturated (Figure 1c) oxygen sites in the $Ti_3C_2T_z$ lattice.[35,36] The notation $x$ in $TiO_x$ reflects the variable oxidation states of titanium, which originate from incomplete oxidation under controlled etching conditions, and play a key role in the Pd adsorption. Unsaturated O atoms act as Lewis bases and possess lone electron pairs that readily attract protons over a wide pH range. This protonation induces a positively charged surface, thereby enhancing the electrostatic affinity for $PdCl_4^{2-}$ adsorption. To synthesize $TiO_x/Ti_3C_2T_z$ NSs enriched with unsaturated oxygen atoms, $Ti_3AlC_2$ was treated with HF etchants of varying concentrations, ranging from 5% to 45% (Figures S1–S10 and Notes S1 and S2, Supporting Information). Two key parameters that influence $PdCl_4^{2-}$ adsorption—zeta potential and isoelectric point (IEP)—were measured for each NS (Figure 1d). The properties exhibited a strong dependence on HF concentration, with NSs etched using 15% HF exhibiting the highest IEP, followed by those etched with 5%, 45%, 25%, and 35% HF. Notably, the zeta potential remained stable at ≈37 mV at pH values below four, which served as advantageous for selective Pd recovery.

The relatively low IEP values observed for NSs etched with HF concentrations other than 15% (≈7.2) were attributed to morphological imperfections. As the interaction between the solvent and $TiO_x$ nanoclusters predominantly governs protonation, and consequently, zeta potential, we analyzed the charge distributions of pristine $Ti_3C_2T_z$ MXene and $TiO_2$ nanoclusters using Bader charge analysis (Figure 1e). The oxygen atoms in MXene exhibited a charge of −1.00e, while the internal ($Ti_1$) and surface ($Ti_2$) Ti atoms exhibited positive charges of +1.48e and +1.69e, respectively (Table S1, Supporting Information). The charges of O atoms were similar to those of O atoms in $TiO_2$ anatase (−1.22e),

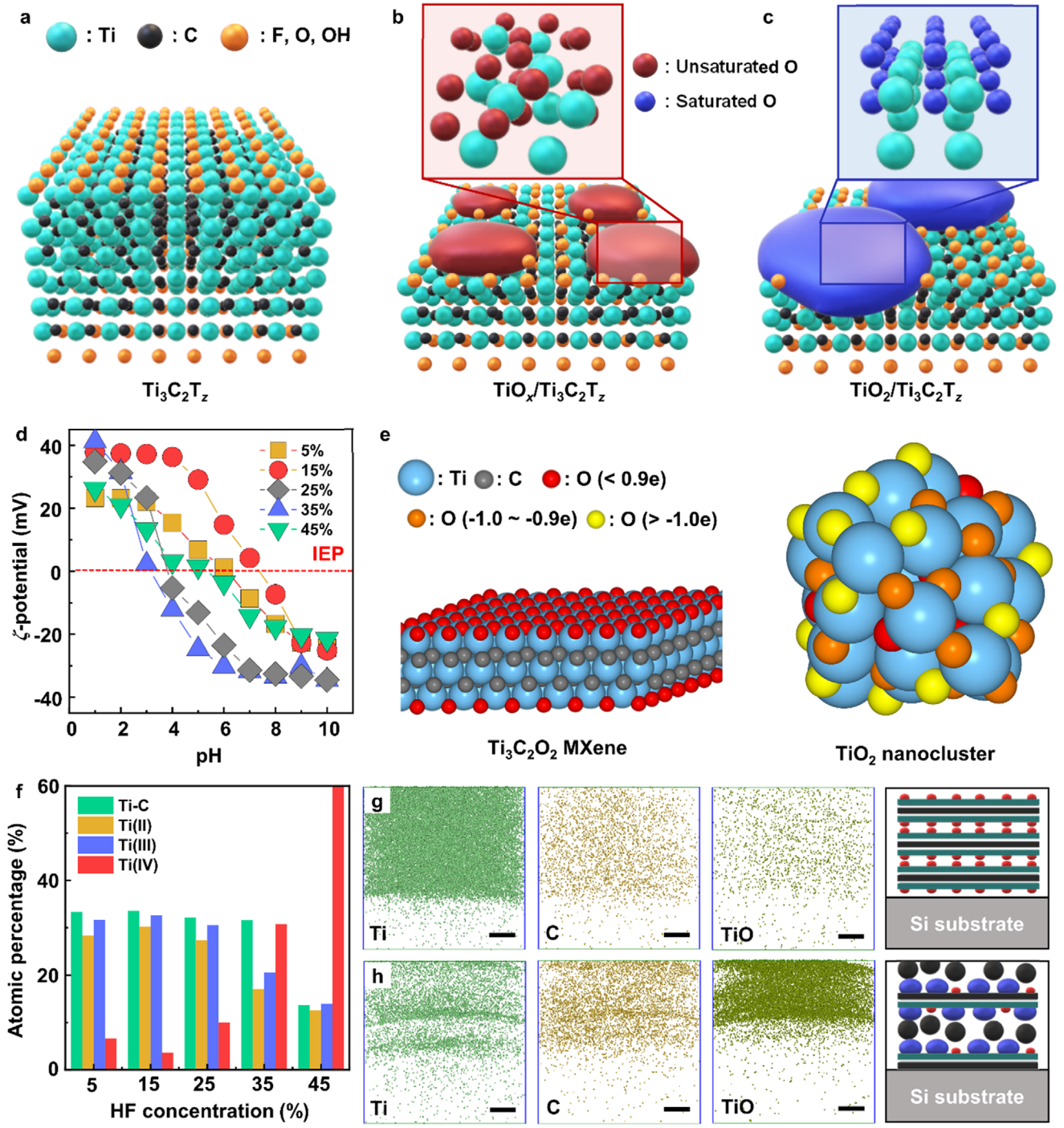


**Figure 1.** Physicochemical properties and protophilicities of the synthesized nanosheets. a–c) Schematics of the synthesized nanosheets (NSs) illustrating different morphologies and surface O saturation levels with varying concentrations of hydrofluoric acid (HF) solution. (a) $Ti_3C_2T_z$, (b) $TiO_x/Ti_3C_2T_z$, and (c) $TiO_2/Ti_3C_2T_z$. d) Zeta-potential values of the $Ti_3C_2T_z$ NSs prepared with different HF concentrations for Al etching, according to pH levels in a range of 1–10. The red dashed line indicates the isoelectric points (IEP). e) The optimized structures and corresponding charge distribution of MXene (left) and nanocluster (right) with respect to oxygen atoms. f) Atomic percentage of the $TiO_x/Ti_3C_2T_z$ NS as a function of HF concentration. g, h) Ionic and elemental distribution analysis using atomic probe tomography (APT) of NSs etched with HF solutions of (g) 15% and (h) 35% and stacked on the specimen, as depicted in the insets at the bottom. Scale bars are 5 nm.

indicating the O atoms in pristine MXene were nearly saturated. Thus, pristine MXene exhibited a low proton affinity owing to the saturation of O atoms, which was consistent with experimental measurements.[37]

The charges of Ti and O atoms in nanoclusters are widely distributed, depending on their coordination environments. Unlike pristine MXene or $TiO_2$ anatase crystals, Ti and O atoms in the nanoclusters that formed on the MXene surface exhibited greater unsaturation, resulting in a broader charge distribution that varied with synthesis conditions, particularly HF concentration.[38] $TiO_2$ nanoclusters exhibited various IEP values depending on their surface morphology.[39] Surface O atoms possessed fewer electrons than those located inside the nanoclusters, as shown inFigure 1e. Consequently, Ti atoms on the lattice surface possessed more electrons than those within the nanoclusters (Figure S11, Supporting Information). These unsaturated surface O atoms, with lower electron density, exhibited high proton affinity, causing a high zeta potential under relatively high pH conditions.[40] This elevated zeta potential corresponded to a high IEP (Figure 1d), thereby enhancing the electrostatic attraction of $PdCl_4^{2-}$. Additionally, electron distribution analysis revealed that surface Ti atoms were more readily accessible for electron transfer, making the NSs more favorable for redox reactions. Contrarily, excessive oxidation of NSs led to the formation of coarse $TiO_2$ crystals with fully saturated O atoms (Figure 1c).

To confirm the influence of surface chemistry of MXenes, which varied with the number of coordinating metal ions depending on HF concentration, on the saturation of O atoms, we analyzed the Ti2*p* X-ray photoelectron spectroscopy (XPS) spectra of the NSs (Figure S12, Supporting Information). The 15%-HF-etched NS exhibited the lowest Ti(IV) content and highest Ti(II) and Ti(III) contents, indicating the presence of unsaturated O atoms. As the HF concentration increased over 25%, the area ratio of the Ti(IV) peak at a binding energy of 458.9 eV increased, consistent with the formation of fully saturated O atoms (i.e., $TiO_2$) due to excess oxidation and associated degradation, as further confirmed by the atomic-scale analysis described later (Figure 1f).[41] Furthermore, the peaks at 530.8 and 532.0 eV in the O 1*s* spectrum (Figure S13a, Supporting Information)—attributed to O atoms replaced by F in the $TiO_2$ lattice and surface hydroxyl groups, respectively—suggested that the coordination of saturated O decreased due to the strong Ti–F bonding, indicated by the strong asymmetric peak at 684.3 eV in the F1*s* spectrum (Figure S13b, Supporting Information).[42] Meanwhile, the disappearance of the Al2*p* peak at 15% HF demonstrated the successful exfoliation without Al residues, indicating a critical balance in HF concentration (Figure S13c, Supporting Information). These results suggest that 15% HF enables controlled etching, leading to uniformly distributed $TiO_x$ nanoclusters with a high fraction of Ti(II) and Ti(III), whereas HF concentrations ≥25% trigger uncontrolled oxidation, resulting in the formation of thick $TiO_2$ layers and Ti–C bond degradation. This transition is consistent with the oxidation mechanism reported by Cao et al.,[43] where etching-induced structural defects accelerate self-propagating $TiO_2$ growth, highlighting ≈25% HF as a critical threshold beyond which irreversible degradation dominates.

The detailed composition and bonding states of NSs etched with varying HF concentrations were analyzed using atomic probe tomography (APT), which provided 3D compositional mapping at sub-nanometer resolution (Figures S14–S16 and Note S3, Supporting Information). The protophilic property of 15%-HF-etched NSs was attributed to the presence of small, uniformly distributed $TiO_x$ nanoclusters on the $Ti_3C_2T_z$ NS surface, as previously revealed by the charge distribution analysis. Reconstructed 3D atom distribution maps of the sample revealed a homogeneous distribution of Ti, C, and TiO throughout the structure, indicating that the intrinsic architecture of the $Ti_3C_2T_z$ NS was maintained intact while simultaneously forming $TiO_x$ nanoclusters (Figure 1g). Conversely, the 35%-HF-etched NSs exhibited excessive oxidation, leading to the dissociation of Ti atoms between NSs and the C atom aggregation, indicative of coarse $TiO_2$ crystal formation (Figure 1h). The observation was consistent with the dynamic growth of $TiO_2$ particles within the $Ti_3C_2T_z$ lattice, which exhibited diameters of several tens of nanometers due to the oxidative process.[43] The accumulated $TiO_2$ potentially contained a higher proportion of fully saturated surface O atoms, thereby reducing the zeta potential. Considering its highly protophilic characteristics and structural stability across a wide pH range, the 15%-HF-etched NS was selected as the optimal $TiO_x/Ti_3C_2T_z$ NS.

### 2.2. Pd Recovery Mechanism

To investigate the recovery mechanism of $PdCl_4^{2-}$ on $TiO_x/Ti_3C_2T_z$ NSs, we analyzed $TiO_2/Ti_3C_2T_z$ NSs after Pd adsorption (Pd/NS) under acidic conditions using various analytical tools. The XPS spectrum of Pd/NSs for Pd3*d* exhibited two deconvoluted peaks corresponding to ionic Pd(II) and reduced Pd(0) states, with respective fractions of 17.9% and 82.1% (**Figure 2a**; Table S2, Supporting Information). Combined with the zeta potential analysis, the obtained results confirmed that $PdCl_4^{2-}$ was electrostatically attracted to the positive zeta potential of the unsaturated O atom, followed by the reduction of most Pd(II) ions to Pd(0) NPs via electron transfer facilitated by Ti (Figure S17, Supporting Information).

The XPS spectrum of Pd/NSs for O1*s* (Figure 2b) indicated that a hydroxyl group (–OH) contributed to the reduction of Pd(II) ions adsorbed on the $TiO_x/Ti_3C_2T_z$ NSs by donating electrons. The C–Ti–OH groups were oxidized to C–Ti–O and/or Ti–O during reduction by the Pd(II) ions (Figure S18, Supporting Information). Furthermore, the XPS Ti2*p* spectra of Pd/NSs revealed that the peaks related to Ti–C, Ti(II), and Ti(III) significantly decreased (Figure 2c), whereas that corresponding to Ti(IV) increased, suggesting a redox interaction between the Pd(II) ions and $TiO_x/Ti_3C_2T_z$ NS. This observation is consistent with previous studies reporting that low-valence Ti species (Ti(II)/Ti(III)) on $Ti_3C_2T_x$ MXene surfaces serve as intrinsic electron donors that reduce Pd(II) ion via in situ redox processes, accompanied by the oxidation of Ti to Ti(IV).[44]

The XPS spectrum for F1*s* (Figure 2d) revealed that the peaks at 684.3 and 685.7 eV, corresponding to Ti–F and C–F, shifted to higher binding energies at 684.7 (+0.4 eV) and 685.9 (+0.2 eV) eV, respectively (Figure S19, Supporting Information). This shift suggested that F atoms near the O atoms increased the overall polarity of the $TiO_x/Ti_3C_2T_z$ NS lattice by polarizing the

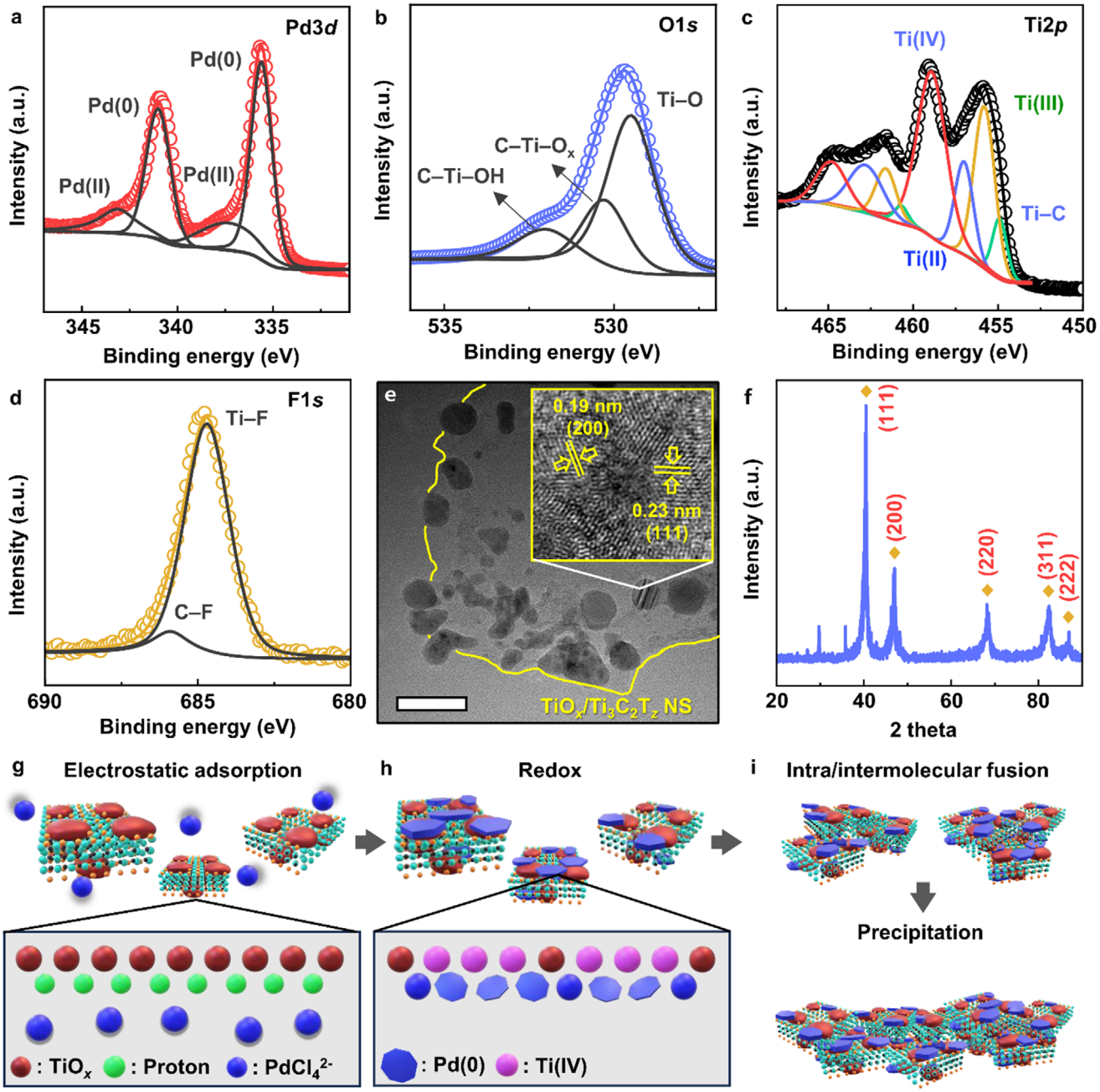


**Figure 2.** Pd recovery mechanism of $TiO_x/Ti_3C_2T_z$ NS. a–d) High-resolution XPS spectrum of (a) Pd3*d*, (b) O1*s*, (c) Ti2*p*, and (d) F1*s* for $TiO_x/Ti_3C_2T_z$ NSs after Pd adsorption. e) TEM image of $TiO_x/Ti_3C_2T_z$ NS after Pd adsorption. Scale bar is 100 nm. Inset is a high-magnification TEM image of $Ti_3C_2T_z$ NS after Pd adsorption, producing the crystal structure information extracted from the lattice fringes. f) XRD pattern of $TiO_x/Ti_3C_2T_z$ NSs after Pd adsorption. g–i) Produced Pd adsorption mechanism of $TiO_x/Ti_3C_2T_z$ NSs through (g) electrostatic adsorption, (h) redox reaction, and (i) coagulation.

neighboring O atoms; thus, the enhanced polarity contributed to the more efficient reduction of Pd(II) ions.[45,46]

High-resolution transmission electron microscopy (HRTEM) images of the crystals grown from Pd(II) (Figure 2e) revealed lattice fringes that matched the X-ray diffraction (XRD) patterns (Figure 2f). The (002) peak disappeared in the XRD pattern after Pd adsorption due to the uniform and dense deposition of reduced Pd NPs on the $TiO_x/Ti_3C_2T_z$ nanosheet surfaces, which obscured the characteristic MXene signals. The average diameter of Pd NPs was measured to be 9.08 nm (Figure S20, Supporting Information). Field-emission scanning electron microscopy (FESEM) images of the Pd/NS revealed that the surface of the $TiO_x/Ti_3C_2T_z$ NSs was uniformly covered with Pd NPs (Figure S21, Supporting Information). This aggregated morphology is attributed to the nature of $PdCl_4^{2-}$ coordination: as a multidentate ligand, $PdCl_4^{2-}$ requires simultaneous binding with multiple functional groups. Due to the spatial constraints on individual nanosheets, adjacent $TiO_x/Ti_3C_2T_z$ NS cooperatively chelate

$PdCl_4^{2-}$, promoting nanosheet-to-nanosheet proximity and aggregation. Upon subsequent Ti-mediated reduction, metallic Pd nanoparticles form at these interfacial sites, effectively bridging the nanosheets and leading to intermolecular fusion.[47] This fusion process results in a stable aggregate structure that facilitates both collection and catalytic performance.

Under acidic conditions, Pd-chloro anions were adsorbed on the positively charged surface of the $TiO_x/Ti_3C_2T_z$ NSs through electrostatic attraction (Figure 2g). Further, the adsorbed Pd(II) ions were reduced to Pd(0) NPs on the NS surface, possessing a lower reduction potential than Pd(II) (Figure 2h).[48,49] This self-reduction process aligns with previous studies showing that low-valence titanium species (e.g., Ti(II) and Ti(III)) in MXene, which possess lower redox potentials than Cu(II), act as key reducing agents facilitating electron transfer.[48] The lattice mismatch between the Pd NPs and the $Ti_3C_2T_z$ substrate induces Volver-Weber mode deposition, which inhibits NPs agglomeration and results in uniformly dispersed NPs with sizes of a few nanometers. Additionally, Ti vacancies on the MXene surface likely serve as preferential nucleation and anchoring sites for metal atoms.[50] EXAFS results from this study further support this interaction by showing that metal atoms preferentially nucleate at defect or vacancy sites on MXene. These local bonding configurations — characterized by strong covalent interactions such as M–C and M–O bonds (with O-terminal atoms)—stabilize atomically dispersed species at low loadings and, at higher loading, promote uniform NPs formation. These findings suggest that MXene not only functions as a stable support but also enables precise control over the nucleation, growth, and spatial distribution of metallic NPs. In our system, the controlled reduction and dispersion of Pd NPs contribute to the intermolecular fusion of Pd-loaded NSs, possibly due to hydrogen bonding or electrostatic interactions between adjacent NSs. This adsorption between the nanocluster surface and Pd(II) ions facilitated rapid electron transfer, promoting the growth of larger Pd(0) NPs. This hybrid reaction of Pd adsorption–reduction generated Pd/NS precipitates, facilitating their easy collection (Figure 2i).

### 2.3. Pd Recovery Performance

The optimal adsorbent dose and pH range for Pd recovery using the $TiO_x/Ti_3C_2T_z$ NS were determined through isothermal adsorption experiments and hydrodynamic morphology analysis (Figures S22–S24 and Note S4, Supporting Information). Commercial carbon black (CB), a widely used support material for Pd catalysts, was taken as a reference to evaluate the recovery performance during Pd upcycling and recycling.[51]

During the experiment, $TiO_x/Ti_3C_2T_z$ NSs demonstrated exceptional Pd recovery efficiency ($R_e$) of ≈100%, even at a $C_i$ of 100 μg $L^{-1}$, significantly outperforming CB, which achieved ≈18.2% Pd recovery (**Figure 3a**). This superior performance was attributed to the high reducibility and substantially higher zeta potential of the $TiO_x/Ti_3C_2T_z$ NSs (≈37 mV) compared to that of CB (≈3 mV) at pH 1 (Figure S25, Supporting Information). After Pd recovery, the densities of the $TiO_x/Ti_3C_2T_z$ NSs and CB increased to ≈140% and 11%, respectively (Figure S26, Supporting Information), indicating the significant immobilization of Pd NPs via redox reaction on the $TiO_x/Ti_3C_2T_z$ NS surface. Contrarily, CB powder exhibited only ionic Pd(II) peaks (100%) (Figure S27, Supporting Information), suggesting that Pd(II) was adsorbed solely through electrostatic interactions.

The precipitation behavior of $TiO_x/Ti_3C_2T_z$ NSs and CB was characterized by monitoring the changes in their hydrodynamic diameters ($H_R$) with increasing contact time ($t$) in the Pd(II) solution (Figure 3b). The $H_R$ of $TiO_x/Ti_3C_2T_z$ NSs increased rapidly and plateaued within 60 min. Notably, $TiO_x/Ti_3C_2T_z$ NSs formed microscale precipitates with an average size of ≈9.5 μm, which quickly sank to the bottom and were easily collected by simple membrane filtration (Figure S28, Supporting Information). Therefore, $TiO_x/Ti_3C_2T_z$ NSs facilitated the intermolecular fusion of multiple NSs. Conversely, CB demonstrated only a slight increase in $H_R$ after Pd(II) adsorption, as its Pd adsorption mechanism mainly relied on electrostatic interactions, which were less effective for inducing precipitation.

The adsorption isotherm curve of $TiO_x/Ti_3C_2T_z$ NSs for Pd(II) was well fitted to the Freundlich and Redlich–Peterson models ($R^2 \geq 0.97$) better than the Langmuir model ($R^2 = 0.88$) (Figure 3c; Table S3, Supporting Information). Thus, Pd(II) was adsorbed primarily via pseudo-multilayer adsorption. The maximum adsorption capacity ($q_m$) of the $TiO_x/Ti_3C_2T_z$ NSs was empirically determined as 1983.3 mg $g^{-1}$. The adsorption capacity of the $TiO_x/Ti_3C_2T_z$ NSs attained equilibrium within 60 min (Figure 3d). The pseudo-second-order model best fitted the kinetic adsorption data for Pd(II), with a better $R^2$ value than the pseudo-first-order and Elovich models (Table S4, Supporting Information). Thus, the rate-limiting step of Pd adsorption on $TiO_x/Ti_3C_2T_z$ NSs was chemisorption.[52]

Compared to other reported Pd adsorbents, $TiO_x/Ti_3C_2T_z$ NSs exhibited a significantly higher $q_m$ value and faster adsorption equilibrium time for Pd(II) (Figure 3e; Table S5, Supporting Information). The rapid and high-capacity recovery of Pd was attributed to its strong reduction capability, coupled with efficient adsorption via robust electrostatic interactions.

### 2.4. Practical Applicability

The Pd recovery selectivity using $TiO_2/Ti_3C_2T_z$ NSs prepared with varying HF concentrations was tested in simulated industrial wastewater containing various co-existing heavy metal ions such as Cu(II), Ni(II), Mg(II), Ca(II), K(I), and Na(I) (**Figure 4a**).[52] The 15%-HF-etched NSs demonstrated ≈100% $R_e$ for Pd(II) while exhibiting negligible $R_e$ of less than 1% for other ions, underscoring their exceptional Pd recovery performance and selectivity. Conversely, the lower or negative zeta potential values of the other NSs indicated poor Pd adsorption selectivity and efficiency against co-existing heavy metal cations.

We further evaluated the practical applicability of the $TiO_x/Ti_3C_2T_z$ NS for Pd recovery from the leachates of spent Pd catalysts (Figure 4b–e). Spent Pd catalysts, considered major secondary resources for Pd, were typically supported on γ-alumina ($Al_2O_3$).[53] The total organic C (TOC) concentration in the leachate was 1.42 mg $L^{-1}$, with a metal composition of 10.80 mg $L^{-1}$ for Pd(II) and 4.18 mg $L^{-1}$ for Al(III) (Figure S29, Supporting Information). $TiO_x/Ti_3C_2T_z$ NSs achieved 100% Pd(II) recovery from the leachate without adsorbing co-existing metal ions or organic pollutants (Figure 4f). The selective

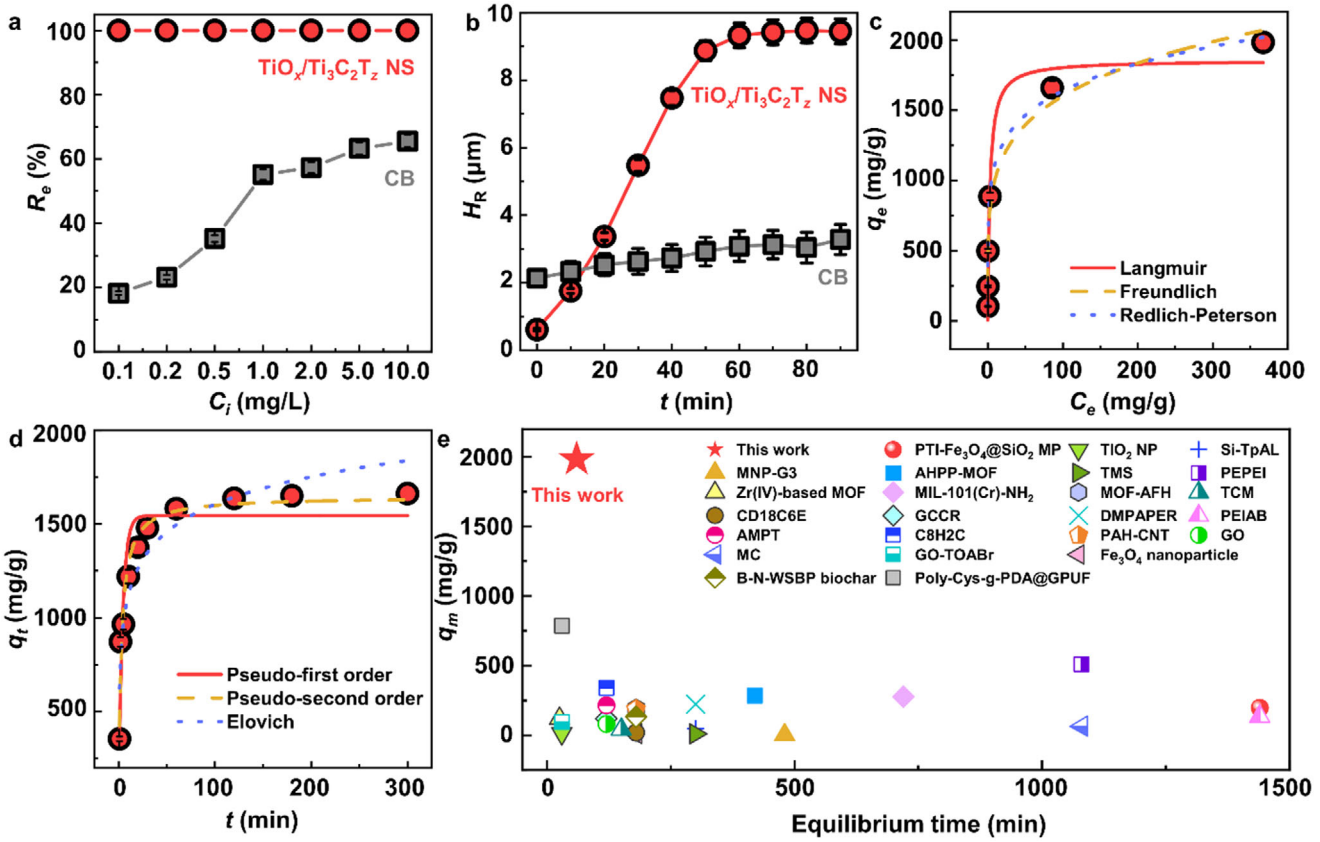


**Figure 3.** Pd recovery performance of $TiO_x/Ti_3C_2T_z$ NS. a) Recovery efficiency ($R_e$) of $TiO_x/Ti_3C_2T_z$ NS for Pd(II) ions, freeze-dried $Ti_3C_2T_z$ (FD_NS), and carbon black (CB) at low initial concentration ($C_i$) in the range 0.1–10.0 mg $L^{-1}$. Solution pH is adjusted to 1. b) Hydrodynamic diameter ($H_R$) of $TiO_x/Ti_3C_2T_z$ NSs during Pd recovery. $C_i$ is 500 mg $L^{-1}$. Solution pH is adjusted to 1. c) Adsorption isotherm curve of $TiO_x/Ti_3C_2T_z$ NS for Pd(II) ion. Solution pH is adjusted to 1. d) Adsorption kinetics curve of $TiO_x/Ti_3C_2T_z$ NS for Pd(II) ion. $C_i$ of Pd is 500 mg/L. e) Adsorption performances of $TiO_x/Ti_3C_2T_z$ NSs compared with those of some of the best-reported adsorbents (Table S5, Supporting Information).

adsorption is attributed to the electrostatic interactions between the $TiO_x/Ti_3C_2T_z$ NS and the metal species. Anionic $PdCl_4^{2-}$ ions are electrostatically attracted to the positively charged NS surface, whereas cathionic Al(III) ions are repelled. To further confirm this mechanism, we introduced ethylenediaminetetraacetic acid (EDTA), which forms stable, negatively charged complexes with Al(III). As the EDTA concentration increased, the zeta potential of the solution became more negative (Figure S30, Supporting Information), indicating successful complexation. Correspondingly, the adsorption of Al-EDTA complexes onto the positively charged NS surface increased (Figure S31, Supporting Information), supporting the conclusion that electrostatic attraction governs the interaction. These results provide experimental validation for the electrostatic mechanism underlying the selective recovery of Pd(II).

Contrarily, commercial CB exhibited a low selectivity for Pd(II) owing to the higher recovery of co-existing Al(III) ions and organic pollutants.

Furthermore, $TiO_x/Ti_3C_2T_z$ NSs were reusable by detaching Pd(II) from Pd/NS. The formed $TiO_2$ in the NS was dissolved in a strong acid, exposing the surface Ti atoms. During this process, interactions with the acidic solution facilitated the partial reduction of Ti(IV) to Ti(III), leading to the formation of new surface chemical species, such as Ti(III)-F and Ti(III)-O (Figure S32, Supporting Information).[54] This transformation was not merely a dissolution process but rather a coupled mechanism involving surface chemical modification and electron transfer (Figure S33 and Note S5, Supporting Information). The considered eluent achieved a desorption efficiency of ≈99.1% (Table S6, Supporting Information). The $TiO_x/Ti_3C_2T_z$ NSs exhibited excellent reusability (Figure 4g), with a much lower reduction (≈1.3%) in $R_e$ per cycle compared to CB (≈4.4%). Pd(II) ions desorbed from Pd/NS were easily recovered through simple evaporation, yielding a high-purity Pd product (99.9%) (Figure 4h).

### 2.5. Electrocatalytic Upcycling

As part of an upcycling strategy for Pd/NS, the catalytic activity for HER was systematically evaluated using electrochemical measurements in 0.1 M $HClO_4$ solution. The influence of Pd intercalation into the NSs on the maximization of active catalytic sites was investigated by comparing HER performance across different catalyst preparation methods (Figures S34 and S35 and Note S6, Supporting Information). The HER polarization curves of the Pd/NS catalysts with weight fractions ranging from ≈5–62 wt.% (5–62-Pd/NS) revealed that $TiO_x/Ti_3C_2T_z$ NSs with the highest Pd content exhibited the lowest

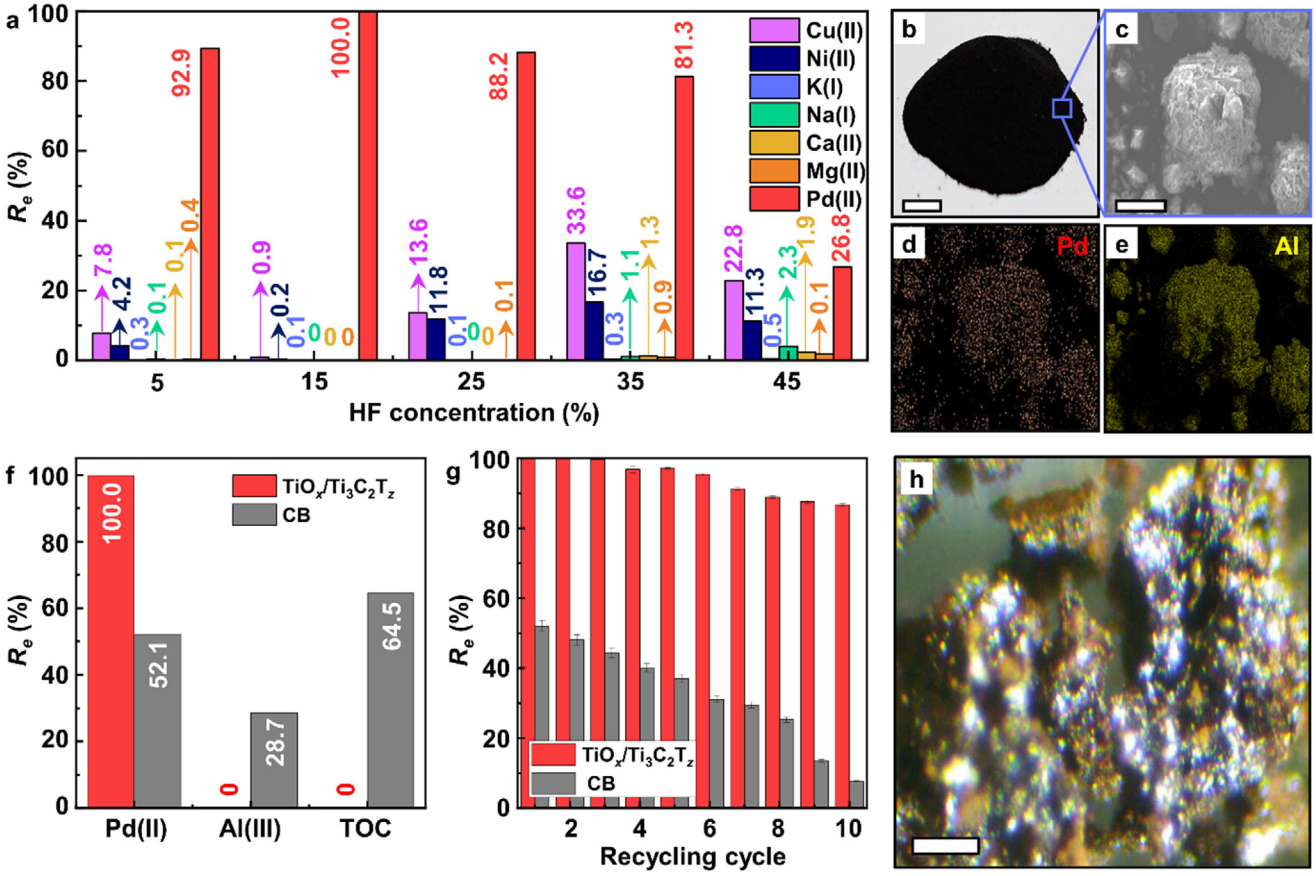


**Figure 4.** Applicability of $TiO_x/Ti_3C_2T_z$ NS for practical Pd recovery. a) Recovery efficiency ($R_e$) of Pd using the $TiO_x/Ti_3C_2T_z$ NS prepared from different HF concentrations with Pd-containing simulated industrial wastewater. The initial concentration ($C_i$) of Pd(II) ion and co-existing metal ions are 1 and 100 mg $L^{-1}$, respectively. The solution pH is not adjusted (≈3.9). b) Real photograph of the spent Pd catalyst. Scale bar is 1 cm. c) FESEM image of the spent Pd catalyst. Scale bar is 20 µm. d, e)FESEM-EDS elemental mapping of the spent Pd catalyst for (d) Pd and (e) Al. f) $R_e$ of $TiO_x/Ti_3C_2T_z$ NS and CB for Pd(II), Al(III), and TOC in a leaching solution from spent Pd catalyst. g) $R_e$ of $TiO_x/Ti_3C_2T_z$ NS and CB for Pd in a leaching solution from spent Pd catalyst during the repetitive Pd adsorption-desorption cycles. h) Optical microscope image of the Pd with 99.9% purity obtained after refinement from the Pd/NS precipitates. Scale bar is 500 µm.

overpotential of 39 mV at a current density of −10 mA $cm^{-2}$ in 0.1 M $HClO_4$ (**Figure 5a**). The mass activities, calculated by dividing current by Pd mass, demonstrated that the Pd mass itself did not entirely determine the catalytic activity. The 62-Pd/NS catalyst exhibited the best performance (≈0.19 A $mg^{-1}$), outperforming other variants with lower Pd content (≈0.16, 0.15, 0.11, and 0.09 A $mg^{-1}$ for 57-Pd/NS, 53-Pd/NS, 47-Pd/NS; and 33-Pd/NS, respectively) (Figures 5b; S36, Supporting Information). The improvement as attributable to enhanced Pd NP intercalation within the $TiO_x/Ti_3C_2T_z$ NS, which facilitated better electrocatalytic performance. Electrochemical impedance spectroscopy (EIS) (Figure S37, Supporting Information) confirmed the distinct variations in the charge-transfer behavior of the Pd/NS catalysts with different Pd weight fractions.

This high catalytic activity was further supported by the slopes of the Tafel plots for the 62–33-Pd/NS catalysts, which demonstrated excellent practical suitability with values below ≈100 mV/dec, outperforming previously reported Pd@MXene-based catalysts.[55,56] Conversely, CB, exhibiting a lower Pd recovery efficiency than $TiO_x/Ti_3C_2T_z$ NSs, demonstrated limited electrochemical activity and poor charge transfer. Notably, 62-Pd/NS exhibited a performance comparable to that of a commercial Pd/C catalyst (Premetek, 40 wt.% Pd on Vulcan XC-72), suggesting that the upcycled Pd/NS catalyst promoted promising catalytic activity (Figure S38, Supporting Information).

Further, we assessed the long-term stability of Pd/NS by conducting a chronopotentiometric (CP) test at −10 mA $cm^{-2}$ for 72 h, revealing negligible changes in potential (Figure 5d). HAADF-STEM imaging and corresponding energy-dispersive X-ray spectroscopy (EDS) mapping showed that the interface between the Pd NPs and the $TiO_x/Ti_3C_2T_z$ NS support remained intact after 72 h of continuous catalytic reaction, with no Pd NP agglomeration or desorption (inset of Figure 5d). These results suggest that the strong interaction between the functional groups on the surface of $TiO_x/Ti_3C_2T_z$ NS support and the Pd NPs prevents agglomeration between Pd NPs and reduces desorption during the electrocatalytic reaction. Also, we confirmed the structural durability of $TiO_x/Ti_3C_2T_z$ NS support by comparing HRTEM images before and after the stability test of Pd/NS catalyst (Figure S39, Supporting Information).

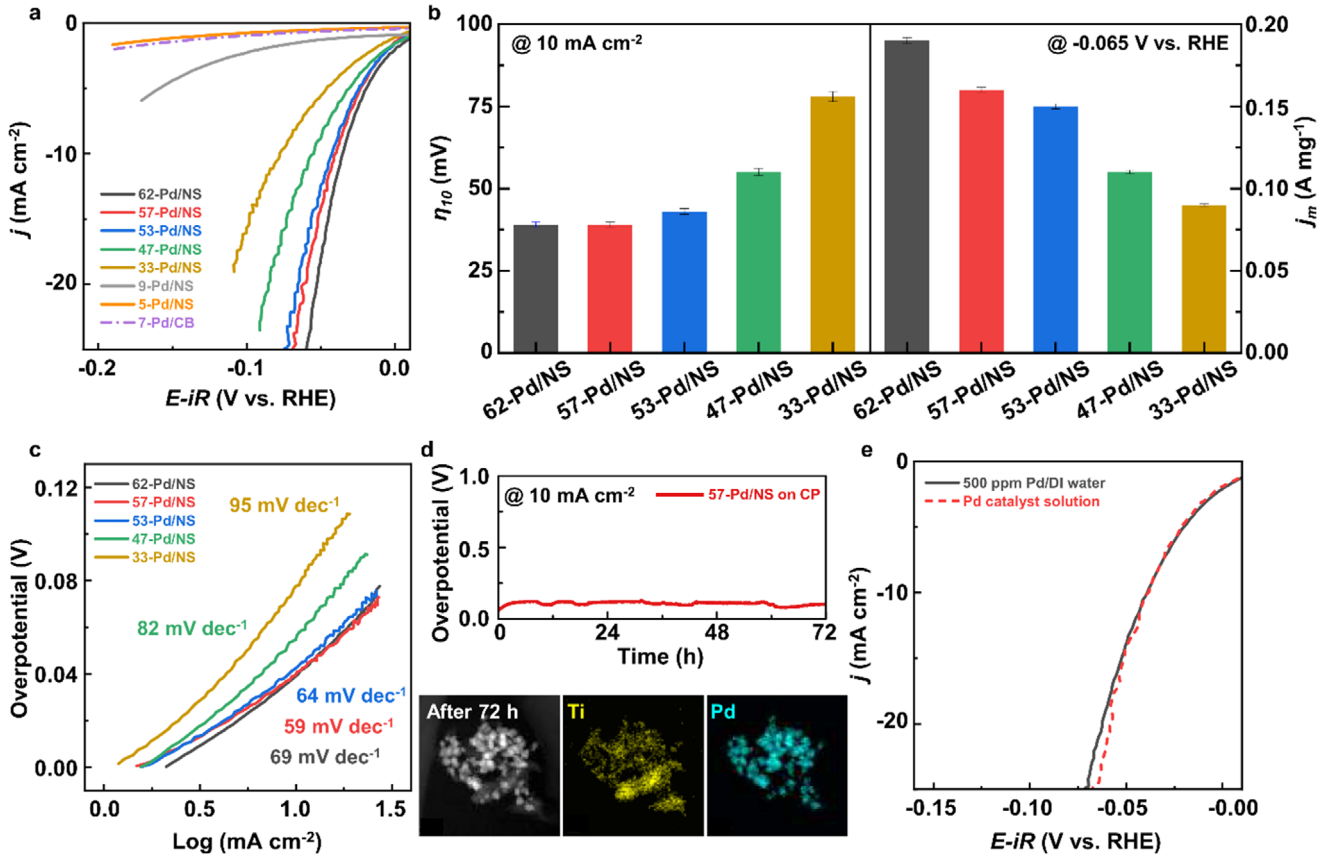


**Figure 5.** Electrochemical performance of $TiO_x/Ti_3C_2T_z$ NS after Pd adsorption in 0.1 M $HClO_4$. a) LSV polarization curves, b) overpotential required at a current density of 10 mA $cm^{-2}$ (left), mass activities (right) of the catalysts at −0.065 $V_{RHE}$, and c) Tafel plots with different Pd weight fractions. d) Chronopotentiometry response at a constant current density of 10 mA/$cm^2$ of 57-Pd/NS deposited on carbon paper. The inset shows TEM images and corresponding EDS mapping results of 57-Pd/NS after the potential cycles. e) LSV polarization curves showing similar HER performance of Pd/NSs with adsorbed Pd from different sources.

For a practical evaluation, we investigated the HER performance of Pd/NS obtained from various waste sources. Electrochemical polarization and impedance tests demonstrated that Pd/NS from both standard Pd solutions and spent Pd catalyst leaching solutions with the same Pd concentration exhibited almost identical HER performances (Figures 5e; S40, Supporting Information). Negligible changes in the electrochemical properties were observed, highlighting the selective adsorption capability of the charge-controlled $TiO_x/Ti_3C_2T_z$ NS or Pd(II) ions, even in the presence of co-existing ions from the catalyst leaching solution. These findings underscore the potential of upcycling Pd/NS as an HER catalyst for various industrial wastewater streams containing Pd(II) ions.

## 3. Conclusion

In this study, we demonstrated the exceptional potential of $TiO_x/Ti_3C_2T_z$ NSs for Pd recovery, upcycling, and recycling. The synthesized $TiO_x/Ti_3C_2T_z$ NSs featured $TiO_x$ nanoclusters with unsaturated O atoms that exhibited high proton affinity. Thus, the IEP at higher pH levels increased, facilitating the electrostatic adsorption of $PdCl_4^{2-}$. Consequently, the highly positively charged surface (i.e., ≈ +37 mV zeta potential) of the $TiO_x/Ti_3C_2T_z$ NS remained stable over a wide pH range of 1–4, enabling selective $PdCl_4^{2-}$ adsorption in both model acidic industrial wastewater and real-world leachate from spent Pd catalysts. The strong adsorption–redox properties of the $TiO_x/Ti_3C_2T_z$ NS for Pd(II) promoted intermolecular fusion, enhancing Pd reduction and yielding large precipitates that were readily collected via membrane filtration. This multi-layer immobilization of Pd NPs on $TiO_x/Ti_3C_2T_z$ NS significantly improved adsorption capacity and kinetics, with higher selectivity for Pd(II) than commercial CB and other laboratory-fabricated Pd adsorbents. The collected Pd/NS precipitates were separated into high-purity Pd particles and intrinsic $TiO_x/Ti_3C_2T_z$ NS adsorbents or directly applied as electrocatalysts for HER in hydrogen purification and storage. Remarkably, $TiO_x/Ti_3C_2T_z$ NSs retained ≈87% of their maximum Pd adsorption capacity even after ten adsorption–desorption cycles. We successfully elucidated the Pd adsorption mechanism, confirming the high capacity, selectivity, and reusability of $TiO_x/Ti_3C_2T_z$ NSs as a standalone Pd adsorbent. These results underscore the upcycling efficiency of Pd/NS for HER and its practical reusability.

Our findings suggest that precise control over the physicochemical structure of MXenes can enable the development of high-performance adsorbents for recycling valuable resources or

removing hazardous substances from industrial wastewater, e-waste leachates, spent catalysts, and batteries. This study opens new avenues for sustainable recycling technologies, contributing to circular economy strategies and the conservation of critical resources.

## 4. Experimental Section

*Nanosheet Synthesis*: TiC (99.5%, particle size: 2 µm, Alfa Aesar, USA), Ti (99.5%, mesh size: 325, Alfa Aesar), and Al (99.5%, 325 mesh, Alfa Aesar) powders were purchased and utilized without additional purification steps. MAX ($Ti_3AlC_2$) powder was synthesized by ball-milling a mixture of TiC, Al, and Ti powders in a molar ratio of 2:1:1 under an $N_2$ gas environment at 25 °C. The powder mixture (5 g) was placed in a 15 mL alumina crucible, which was then heated at a rate of 5 °C $min^{-1}$ until reaching 1450 °C, followed by holding at this temperature for 2 h under an Ar flow rate of 3 L/flow. The sintered powder was milled and sieved through a 325-mesh screen.

The Al layers in the $Ti_3AlC_2$ powder were removed to enhance the specific surface area and immobilize the hydrophilic functional groups. The $Ti_3AlC_2$ powder (1 g) was introduced into 20 mL of hydrofluoric acid (HF, ACS reagent, Acros Organics, Belgium) solution of different concentrations (5%, 15%, 25%, 35%, and 45%), and the mixture was agitated for 24 h at 25 °C. The resulting $Ti_3C_2T_z$ flakes were rinsed with deionized (DI) water by centrifugation (3500 rpm, 5 min per cycle) until the pH of the supernatant reached six. Subsequently, the intercalation of the $Ti_3C_2T_z$ flakes was performed using tetramethylammonium hydroxide (TMAOH, 25 wt.% in $H_2O$, Sigma-Aldrich). Initially, 10 mL of intercalant with 50 mL of DI water was added to the prepared sediments and stirred for 48 h at 25 °C, then washed with DI water through centrifugation to eliminate the intercalant (12 000 rpm, 10 min per cycle). The rinsing procedure was repeated by adding water to wash away any remaining reagent thoroughly. The sediments were post-treated by thermal drying, freeze drying, and dispersion in DI water via ultrasonication for 1 h.

*Atomic Probe Tomography (APT)*: Needle-shaped APT specimens were prepared using a dual-beam focused ion beam (FIB, Nova 600 NanoLab) equipped with a Ga ion source and a micromanipulator. Specimens were prepared by the drop-casting of NSs delaminated in individual batches with varying HF concentrations (15%, 25%, and 35%). The drop-cast NSs on Si substrates were coated with Cr using focused ion beam (FIB) deposition in the region of interest (ROI) following the lift-out and sharpening protocol.[57] Specifically, a Cr lamella was positioned 10 µm above the well-dispersed NSs, followed by hemispherical circle pattern milling to create a protective Cr coating layer on the nanosheet surfaces. Analysis was performed at a laser power energy of 60 pJ and a laser band of 355 nm at a base temperature of 50 K.

The specimens were measured using a local electrode atom probe (LEAP 4000X HR, AMETEK) by applying a laser pulse energy of 60 pJ with ultraviolet (wavelength = 355 nm) laser pulses, a pulse repetition rate of 125 kHz, and a detection rate of 0.3%. Data were reconstructed and analyzed using interactive visualization and analysis software packages (IVAS 6.3, AP Suite 6.0, AMETEK).

*Single-Component Batch Pd Recovery Tests*: Pd stock solutions at predetermined Pd ion concentrations (1000 mg $L^{-1}$ standard solution, Sigma-Aldrich) were prepared by diluting the Pd standard solutions with DI water while adjusting the pH to 1–3 using aqueous 1 N HCl (Sigma-Aldrich) and 1 N NaOH (Sigma-Aldrich) solutions. $TiO_x/Ti_3C_2T_z$ NSs (0.2 g $L^{-1}$) were introduced in the Pd solutions and stirred at 200 rpm at 25 °C for 24 h. CB (Vulcan XC-72) was used as a counter sample by subjecting it to the same conditions for comparison. The mixture was filtered through a 0.45-µm-pore membrane, and the supernatant was collected. The Pd concentrations obtained before and after the addition of the adsorbents were determined using inductively coupled plasma optical emission spectrometry (ICP-OES, ICAP 7200, Thermo Scientific, USA). The adsorption capacity at equilibrium ($q_e$, mg/g), which represented the adsorbate mass (mg) per unit of adsorbent mass (g), was calculated as:

$$q_e = \frac{(C_i - C_e) \times V}{M} \quad (1)$$

where $C_i$ and $C_e$ are the initial concentration and the concentration at equilibrium, respectively. $V$ is the solution volume, and $M$ is the adsorbent mass. $R_e$ (%) was calculated as:

$$R_e = \frac{C_i - C_e}{C_i} \times 100 \quad (2)$$

At least three replicates were performed, and the results were averaged.

*Adsorption Selectivity Analysis*: Industrial wastewater containing Pd(II) ions is highly diverse and contains different co-existing metal ions and pH values. Considering that typical wastewater containing Pd(II) ions includes Pd(II), Mg(II), Cu(II), Ni(II), Ca(II), K(I), and Na(I), the simulated solution was prepared using the respective metal standard solution of Pd(II), Mg(II) ($Mg(NO_3)_2{\cdot}6H_2O$, Sigma-Aldrich), Cu(II) ($Cu(NO_3)_2{\cdot}3H_2O$, Sigma-Aldrich), Ni(II) ($Ni(NO_3)_2{\cdot}6H_2O$, Sigma-Aldrich), Ca(II) ($Ca(NO_3)_2{\cdot}4H_2O$, Sigma-Aldrich), K(I) ($KNO_3$, Sigma-Aldrich), and Na(I) ($NaNO_3$, Sigma-Aldrich). The initial concentrations of the Pd(II) ions and co-existing metal ions were 1 and 100 mg/L, respectively. The pH of the solution was not adjusted to mimic industrial wastewater. The $TiO_x/Ti_3C_2T_z$ NS (0.2 g/L) was added to the simulated solution, stirred at 200 rpm for 3 h, and filtered through a 0.45-µm-pore membrane filter. The metal ion concentrations in the permeate solutions were measured using ICP-OES.

*Pd Recovery in a Leaching Solution from Spent Pd Catalyst*: Spent Pd catalysts (Sigma-Aldrich, USA) were obtained after use in hydrogenation reactions. The leachate solution was prepared by immersing the spent Pd catalyst (20 g) in aqua regia (500 mL) for 3 days. The mixture was filtered through a 0.45-µm-pore membrane to remove undissolved solids and further diluted to obtain 1 L solution with DI water while adjusting pH to 1 using a 1 N NaOH aqueous solution. $TiO_x/Ti_3C_2T_z$ NS (0.2 g $L^{-1}$) were added to the leachate solution and stirred at 200 rpm for 24 h. The mixture was then filtered through a 0.45-µm-pore membrane, and the supernatant was collected. The metal ion concentrations of the solutions obtained before and after the addition of $TiO_x/Ti_3C_2T_z$ NS were measured using ICP-OES. To identify the effect of coexisting organic pollutants on Pd recovery by the $TiO_x/Ti_3C_2T_z$ NSs, TOC concentrations of the solutions obtained before and after the addition of the $Ti_3C_2T_z$ NSs were measured using a TOC analyzer (TOC-L, Shimadzu, Japan).

*Pd Refinement*: The collected Pd/NS precipitates were introduced into a 0.3 M thiourea (>99.0%, Sigma-Aldrich) in 0.5 M HCl solution at 25 °C for 24 h. The remaining precipitate was separated by centrifugation at 3500 rpm for 5 min per cycle for reuse. The supernatant was transferred to a vial, to which an HCl (37%) aqueous solution (10 mL) was added, and the obtained solution was heated to 60 °C and stirred at 200 rpm for 24 h to enable the complete evaporation of the HCl solution. The resulting particles were washed thrice with DI water to obtain Pd particles. The collected Pd particles were dissolved in aqua regia, and their concentrations in solution ($C$) were analyzed by ICP-OES to determine their purity as:

$$\text{Purity } (\%) = \frac{m}{V_{regia} \times C} \times 100 \quad (3)$$

where $m$ is the mass of the Pd particles and $V_{regia}$ is the volume of aqua regia.

*Regeneration of $TiO_x/Ti_3C_2T_z$ NS*: The filtrated Pd/NS precipitate was added to the aqueous solution containing thiourea (0.3 M) and HCl (0.5 M) at 25 °C for 24 h. The filtered $TiO_x/Ti_3C_2T_z$ NS was freeze-dried and then reused to repeat the adsorption-desorption process.

*Nanosheet Preparation and Electrochemical Characterization of HER Catalysts*: Catalyst inks were prepared by mixing 10 mg of catalyst and 20 µL Nafion solution (5 wt.%) in solution of 1 mL of water/ethanol (99.9%)

mixture solution (volume ratio of 1:1). Then 5 µL of the catalyst ink containing 50 µg of catalyst (10 $mg_{catalyst}$/mL) was deposited onto a glassy carbon (GC) disk (0.194 $cm^2$ area) of a rotating disk electrode (RDE, Autolab) by drop-casting. All electrochemical measurements were conducted using a three-electrode electrochemical cell on a potentiostat (Autolab PGSTAT204 electrochemical workstation) and a rotator (2,000 rpm, Autolab) at 25 °C under 1 bar. Ar gas purged 0.1 M $HClO_4$ (70 wt.%, Aldrich) was used as the electrolyte. Linear sweep voltammetry (LSV) with a scan rate of 5 mV $s^{-1}$ was conducted using an Ag/AgCl (saturated with KCl filling solution, Autolab) electrode as the reference electrode, an RDE with catalysts as the working electrode, and a glassy carbon rod (Autolab) as the counter electrode. Prior to the electrochemical measurements, RDE was reductively cleaned by a cycle process with the potential ranging from 0.05 and 1 $V_{RHE}$ for 20 cycles at a scan rate of 200 mV $s^{-1}$. The potentials were calibrated to the reversible hydrogen electrode (RHE) as:

$$E_{RHE}\,(V) \;=\; E_{app}\;(V) + E^{\circ}_{Ag/AgCl} + 0.0591\;(V) \times pH \tag{4}$$

where $E_{app}$ is the applied potential versus the Ag/AgCl reference electrode, and $E^{\circ}_{Ag/AgCl}$ is the standard potential versus the normal hydrogen electrode of the Ag/AgCl reference electrode (0.196 V).

To measure the solution resistance for *iR*-correction and charge transfer resistance of catalysts, electrochemical impedance spectroscopy (EIS) measurements were conducted at 0 $V_{RHE}$ in the frequency range of 100 kHz to 0.1 Hz and amplitude of 10 mV. The double layer capacitance ($C_{dl}$) of the catalysts was determined by measuring the cyclic voltammograms (CVs) for a small potential range of 0.5–0.6 $V_{RHE}$ with a scan rate of 20 to 320 mV $s^{-1}$. The corresponding current ($\Delta I/2$ at 0.55 $V_{RHE}$) was consistent with the scan rate, and the slope of the linear fitting was the $C_{dl}$. The mass activity of the Pd/NS was calculated as:

$$j_m = \frac{i@-0.065\ V}{m} \tag{5}$$

where *i@-0.065 V* is current (A) at −0.065 $V_{RHE}$ and *m* is the mass of the Pd metal on NS. A long-term stability test was conducted by performing chronopotentiometry CP) measurements at −10 mA $cm^{-2}$, considering the same electrolyte and electrode conditions as in the LSV measurement, with the only difference being the substrate used, which was carbon paper (1 $cm^2$ area) instead of the RDE.

*Sample Characteristics*: The hydrodynamic diameters ($H_R$) of the particulates were analyzed using dynamic light scattering (DLS; ELSZ-2000, Otsuka Electronics, Japan). The surface zeta potentials of the $TiO_x/Ti_3C_2T_z$ NS and CB were measured at different pH values (1−10) using a zeta potential analyzer (ELSZ-2000, Otsuka Electronics, Japan). High-resolution transmission electron microscopy (TEM, Titan TM 80–300, FEI, USA) images were obtained at 200 kV to observe the surface morphologies of the $TiO_x/Ti_3C_2T_z$ NSs before and after Pd recovery. The samples for TEM analysis were dispersed in ethanol on a Ni grid, followed by evaporation. X-ray diffraction (XRD, Rigaku Dmax 2500, Rigaku, Japan) was performed to determine the crystallographic structure of the $TiO_x/Ti_3C_2T_z$ NSs before and after Pd adsorption. The chemical functionalities of the $TiO_x/Ti_3C_2T_z$ NSs before and after Pd adsorption were analyzed using X-ray photoelectron spectroscopy (XPS, PHI5000 VersaProbe, Ulvac-PHI, Osaka, Japan) using a monochromatic Al K$\alpha$X-ray source (protons of 1486.6 eV, 15 kV, and 25 W) to verify the types of surface functionalities. To compensate for the surface-charging effects, all the binding energies of the obtained peaks were referenced to the neutral C 1s peak at 248.8 eV. The XPS Peak4.1 software was used to deconvolute the obtained data using curve fitting. The surface morphologies of $TiO_x/Ti_3C_2T_z$ NSs before and after Pd adsorption were observed using a field emission scanning electron microscope (FESEM, Inspect F50, FEI, USA). The samples for FESEM analysis were put onto a double-sided adhesive carbon tape and sputter-coated with a thin Pt layer (E-1010, Hitachi, Japan) to prevent surface charging. The Brunauer–Emmett–Teller (BET) surface area of the $Ti_3AlC_2$ powder, $TiO_x/Ti_3C_2T_z$ flake, and $TiO_x/Ti_3C_2T_z$ NS were measured by $N_2$ adsorption at 77.245 K using an analyzer (3Flex, Micromeritics, USA).

## Supporting Information

Supporting Information is available from the Wiley Online Library or from the author.

## Acknowledgements

The authors greatly acknowledge the contributions of numerous staff, students, and volunteers who have contributed to this project. Their patience, perseverance, and dedication are greatly appreciated. This research was supported by the National Research Foundation (NRF) funded by the Korean government (MSIT) (Nos. RS-2023-00272602, RS-2023-00209565, and RS-2025-02313809) and KIST institutional program (Nos. 2E33641 and 2E33901) from the Korea Institute of Science and Technology. This study was also partially supported by the Ministry of Environment, Republic of Korea (No. RS-2025-02223005).

## Conflict of Interest

The authors declare no conflict of interest.

## Author Contributions

Y.J. and S.-H.S. synthesized the $Ti_3C_2T_z$ nanosheets with unsaturated $TiO_x$ nanoclusters. J.-W.C., J.Y.K., Y.J., and S.-H.S. conceived the project and supervised the research. Important contributions to the interpretation of the results and conception were made by Y.J., S.-H.S., and K. C. Y.J. and S.-H.S. wrote the paper and are responsible for all data, figures, and text, with assistance from M.J. and K.-S.L. on catalyst measurements and applications. S.K. provided access to commercial software licenses and computational resources (cluster), which were essential for the successful completion of this study. K.C. provided a theoretical idea and designed the adsorbents with unsaturated oxygen atoms. Y.J., S.-H.S., M.J., K.-S.L., and Y.L. performed the experiments and collected the data with the help of K.C., J.Y.K., and J.-W.C. All the authors participated in the discussion of the results and revision of the manuscript and have approved the final version of the manuscript. Y.J. and S.-H.S. contributed equally to this work.

## Data Availability Statement

The data that support the findings of this study are available from the corresponding author upon reasonable request.

## Keywords

coagulation, electrocatalytic upcycling, precious metals, protophilicity, selective recovery, $TiO_x$ decorated MXene, unsaturated oxygen

Received: May 11, 2025
Revised: July 9, 2025
Published online: July 31, 2025

[1] P. Ruiz-Castillo, S. L. Buchwald, *Chem. Rev.* **2016**, *116*, 12564.
[2] C. C. Johansson Seechurn, M. O. Kitching, T. J. Colacot, V. Snieckus, *Angew. Chem., Int. Ed.* **2012**, *51*, 5062.
[3] M. Gazvoda, M. Virant, B. Pinter, J. Košmrlj, *Nat. Commun.* **2018**, *9*, 4814.
[4] A. Chen, C. Ostrom, *Chem. Rev.* **2015**, *115*, 11999.

[5] X. Chen, L. P. Granda-Marulanda, I. T. McCrum, M. T. Koper, *Nat. Commun.* **2022**, *13*, 38.
[6] C. Dong, Z. Gao, Y. Li, M. Peng, M. Wang, Y. Xu, C. Li, M. Xu, Y. Deng, X. Qin, F. Huang, X. Wei, Y.-G. Wang, H. Liu, W. Zhou, D. Ma, *Nat. Catal.* **2022**, *5*, 485.
[7] L. Kuai, Z. Chen, S. Liu, E. Kan, N. Yu, Y. Ren, C. Fang, X. Li, Y. Li, B. Geng, *Nat. Commun.* **2020**, *11*, 48.
[8] A. Remmel, *Nature* **2022**, *606*, 448.
[9] K. S. Song, T. Ashirov, S. N. Talapaneni, A. H. Clark, A. V. Yakimov, M. Nachtegaal, C. Copéret, A. Coskun, *Chem* **2022**, *8*, 2043.
[10] T. S. Nguyen, C. T. Yavuz, *Chem* **2022**, *8*, 1793.
[11] B. J. Glaister, G. M. Mudd, *Miner. Eng.* **2010**, *23*, 438.
[12] P. Nuss, M. J. Eckelman, *PLoS One* **2014**, *9*, 101298.
[13] M. Abbasi, L. Faust, M. Wilhelm, *Adv. Mater.* **2019**, *31*, 1806484.
[14] R. Hussain, M. Saeed, M. Y. Mehboob, S. U. Khan, M. Usman Khan, M. Adnan, M. Ahmed, J. Iqbal, K. Ayub, *RSC Adv.* **2020**, *10*, 20595.
[15] D. I. Kim, G. Gwak, P. Dorji, D. He, S. Phuntsho, S. Hong, H. Shon, *ACS Sustain. Chem. Eng.* **2018**, *6*, 1692.
[16] Y. Chen, M. Xu, J. Wen, Y. Wan, Q. Zhao, X. Cao, Y. Ding, Z. L. Wang, H. Li, Z. Bian, *Nat. Sustain.* **2021**, *4*, 618.
[17] S. R. Cotty, A. Faniyan, J. Elbert, X. Su, *Nat. Chem. Engineer.* **2024**, *1*, 281.
[18] Y. Jung, J. S. Park, K.-W. Jung, Y. G. Ko, J.-W. Choi, *Adv. Fiber Mater.* **2023**, *5*, 2127.
[19] J. Lu, S. Zhang, C. Zhou, X. Wang, B. Lu, Y. Liu, Y. Li, T. N. Hunter, Z. Lu, L. Li, D. Harbottle, Z. Xu, *Sep. Purif. Technol.* **2024**, *332*, 125631.
[20] S. S. Shin, Y. Jung, S. Jeon, S.-J. Park, S.-J. Yoon, K.-W. Jung, J.-W. Choi, J.-H. Lee, *Nat. Commun.* **2024**, *15*, 3889.
[21] W. Wang, S. Zhang, L. Chen, Z. Li, K. Wu, Y. Zhang, Z. Su, X. Yin, M. F. Hamza, Y. Wei, S. Ning, *Sep. Purif. Technol.* **2023**, *322*, 124326.
[22] Y. Bai, L. Chen, L. He, B. Li, L. Chen, F. Wu, L. Chen, M. Zhang, Z. Liu, Z. Chai, S. Wang, *Chem* **2022**, *8*, 1442.
[23] J. Tang, J. Zhao, S. Wang, L. Zhang, M. Zhao, Z. Huang, Y. Hu, *Chem. Eng. J.* **2021**, *407*, 127223.
[24] M. Barakat, M. H. H. Mahmoud, Y. Mahrous, *Appl. Catal., A* **2006**, *301*, 182.
[25] X. Zhang, Z. Chen, Z. Wan, C. Liu, R. He, X. Xie, Z. Huang, *Int. J. Mol. Sci.* **2022**, *23*, 12158.
[26] Y. Jung, U. S. Choi, Y. G. Ko, *J. Mater. Chem. A* **2021**, *9*, 17281.
[27] A. T. Ezhil Vilian, J. N. Tiwari, M. Alhammadi, G. Bhaskaran, S.-K. Hwang, S. Kim, K. Kumar, A. Senthil Kumar, Y. Suk Huh, Y.-K. Han, *Chem. Eng. J.* **2023**, *469*, 144017.
[28] W. Mu, S. Du, X. Li, Q. Yu, H. Wei, Y. Yang, S. Peng, *Chem. Eng. J.* **2019**, *358*, 283.
[29] S. Sukidpaneenid, C. Chawengkijwanich, C. Pokhum, T. Isobe, P. Opaprakasit, P. Sreearunothai, *J. Environm. Sci.* **2023**, *124*, 414.
[30] X. Wang, J. Ding, W. Song, X. Yang, T. Zhang, Z. Huang, H. Wang, X. Han, W. Hu, *Adv. Energy Mater.* **2023**, *13*, 2300148.
[31] C. Cui, R. Cheng, H. Zhang, Y. Ma, C. Shi, B. Fan, H. Wang, X. Wang, *Adv. Funct. Mater.* **2020**, *30*, 2000693.
[32] S. G. Peera, C. Liu, A. K. Sahu, M. Selvaraj, M. C. Rao, T. G. Lee, R. Koutavarapu, J. Shim, L. Singh, *Adv. Mater. Interfaces* **2021**, *8*, 2100975.
[33] Y. Wa, W. Wei, R. Yu, L. Xia, X. Hong, J. Zhu, J. Li, L. Lv, W. Chen, Y. Zhao, L. Zhou, L. Mai, *Adv. Funct. Mater.* **2022**, *32*, 2110910.
[34] Y. Sun, J. Lee, N. H. Kwon, J. Lim, X. Jin, Y. Gogotsi, S.-J. Hwang, *ACS Nano* **2024**, *18*, 6243.
[35] T.-D. T. Carbide, *Science* **2013**, *1241488*, 12158.
[36] Y. Jung, S. H. Seok, K. W. Jung, J. Park, S. Y. Kwon, J. W. Choi, *Small* **2023**, *19*, 2305247.
[37] H. Riazi, M. Anayee, K. Hantanasirisakul, A. A. Shamsabadi, B. Anasori, Y. Gogotsi, M. Soroush, *Adv. Mater. Interfaces* **2020**, *7*, 1902008.
[38] A. Chae, S. Doo, D. Kim, T. Y. Ko, T. Oh, S. J. Kim, D.-Y. Koh, C. M. Koo, *Langmuir* **2022**, *38*, 12657.
[39] D. Liao, G. Wu, B. Liao, *Colloids Surf. A* **2009**, *348*, 270.
[40] P. Venema, T. Hiemstra, P. G. Weidler, W. H. van Riemsdijk, *J. Colloid Interface Sci.* **1998**, *198*, 282.
[41] Y. Zhang, Q. Zhao, B. Danil, W. Xiao, X. Yang, *Adv. Mater.* **2024**, *36*, 2400198.
[42] H.-J. Böhm, D. Banner, S. Bendels, M. Kansy, B. Kuhn, K. Müller, U. Obst-Sander, M. Stahl, *ChemBioChem* **2004**, *5*, 637.
[43] J. He, P. Wu, L. Chen, H. Li, M. Hua, L. Lu, Y. Wei, Y. Chao, S. Zhou, W. Zhu, H. Li, *Chem. Eng. J.* **2021**, *416*, 129022.
[44] J. Zhang, Y. Zhao, X. Guo, C. Chen, C.-L. Dong, R.-S. Liu, C.-P. Han, Y. Li, Y. Gogotsi, G. Wang, *Nat. Catal.* **2018**, *1*, 985.
[45] V. Natu, M. Benchakar, C. Canaff, A. Habrioux, S. Celerier, M. W. Barsoum, *Matter* **2021**, *4*, 1224.
[46] Y. Jung, U. S. Choi, Y. G. Ko, *J. Hazard. Mater.* **2021**, *420*, 126654.
[47] Q. Zhang, J.-A. Wang, Q. Yu, Q. Li, R. Fan, C. Li, Y. Fan, C. Zhao, W. Cheng, P. Ji, J. Sheng, C. Zhang, S. Xie, G. Henkelman, H. Li, *Nat. Synth.* **2025**, *4*, 252.
[48] J. Zhang, K. Sasaki, E. Sutter, R. Adzic, *Science* **2007**, *315*, 220.
[49] J. J. Lingane, *J. Electroanal. Chem.* **1962**, *4*, 332.
[50] S. Li, J. Shu, S. Ma, H. Yang, J. Jin, X. Zhang, R. Jin, *Appl. Catal., B* **2021**, *280*, 119464.
[51] Y. Jung, S.-J. Yoon, J. Byun, K.-W. Jung, J.-W. Choi, *Water Res.* **2023**, *244*, 120543.
[52] S. J. Lee, Y. Yu, H. J. Jung, S. S. Naik, S. Yeon, M. Y. Choi, *Chemosphere* **2021**, *262*, 128358.
[53] Y. Yao, L. Lan, X. Li, X. Liu, Y. Ying, J. Ping, *Small* **2020**, *16*, 1907282.
[54] P. H. Nguyen, D. H. Nguyen, D. Kim, M. K. Kim, J. Jang, W. H. Sim, H. M. Jeong, G. Namkoong, M. S. Jeong, *ACS Appl. Mater. Interfaces* **2022**, *14*, 51487.
[55] D. He, X. Yang, D. Huang, G. Yue, L. Yang, P. Zhao, *Chem. Phys. Lett.* **2022**, *805*, 139942.
[56] S. K. Raj, K. B. Patel, V. Sharma, D. N. Srivastava, V. Kulshrestha, *Energy Fuels* **2023**, *37*, 16856.
[57] T. M. Schwarz, E. Woods, M. P. Singh, X. Chen, C. Jung, L. S. Aota, K. Jang, M. Krämer, S.-H. Kim, I. McCarroll, B. Gault, *Microsc. Microanal.* **2024**, *30*, 1109.